Laser beam shaping with magnetic fluid-based liquid deformable mirrors*

Zhi-Zheng Wu(吴智政)†, Zhu Zhang(张柱), Xiang-Hui Kong(孔祥会), Jun-Qiu Wu(吴君秋), Tao Wang(王韬), Mei Liu(刘梅), and Shao-Rong Xie(谢少荣)

Department of Precision Mechanical Engineering, Shanghai University, Shanghai 200072, *China*

(Received 10 November 2016; revised manuscript received 23 February 2017; published online 17 May 2017)

A new controllable laser beam shaping technique is demonstrated, where a magnetic fluid-based liquid deformable mirror is proposed to redistribute the laser phase profile and thus change the propagation property of the beam. The mirror is driven by an inner miniature actuator array along with a large outer actuator. The inner actuator array is used for deforming the magnetic fluid surface, while the outer actuator is used to linearize the fluid surface response and amplify the magnitude of the deflection. In comparison to other laser beam shaping techniques, this technique offers the advantages such as simplicity, low cost, large shape deformation, and high adaptability. Based on a fabricated prototype of the liquid deformable mirror, an experimental AO system was set up to produce a desired conical surface shape that shaped the incident beam into a Bessel beam. The experimental results show the effectiveness of the proposed technique for laser beam shaping.

Keywords: laser beam shaping, magnetic fluid, deformable mirror, Bessel beam

PACS: 42.15.Dp, 47.65.Cb **DOI:** 10.1088/1674-1056/26/7/074201

1. Introduction

Ever since the invention of laser, due to its high powered, directional, coherent, and monochromatic properties, it has been widely used in industrial, medical, and military fields.[1] However, the typical propagation property of a laser beam is unable to meet some specific requirements in the practical applications such as optical communication, microparticle manipulation, and material processing. To extend the application of the laser technology and improve the efficiency of the laser system, a laser beam shaping technique is needed to convert the incident beam into special beams, such as vortex beam,[2] Bessel beam,[3] focus beam,[4] etc.

A laser beam shaping technique is generally based on the modulation of phase which changes the propagation property of a beam. Researchers originally employed the simple technique of beam aperturing,[5] where the beam is expanded and an aperture is used to select a suitable portion. However, the main disadvantage of this technique is that it causes significant energy loss. To overcome this deficiency, lossless or low-loss shaping techniques are considered. Low-loss beam shaping for laser sources can be broken down into two basic categories.[6] The first is the beam shaping technology based on static optical elements, which include aspheric lenses,[7–9] microlens array,[10,11] birefringent lenses,[12,13] diffractive optical elements,[14,15] axicons,[16] etc. The common goal of these methods is to produce an optical device which modifies the coming beam from a given source to a desired irradiance distribution. However, the static optical elements only produce beams with a specific spatial frequency, hence, the parameters of the beam are fixed, thus it has low adaptability. The second is the beam shaping technology based on adaptive optics, which includes liquid crystal spatial light modulators (SLMs)[17,18] and deformable mirrors (DMs).[19,20] The SLMs are available in both reflective as well as transparent modes, and have the advantage of very high spatial resolution. However, they cannot transmit the beams with wavelengths longer than 1.6 μm.[19] DMs have the important advantages of high throughput and being substantially achromatic, however, most of the DMs are complex and expensive, and normally provide the small stroke deflection less than 30 μm.

The variety of applications with large stroke requirements have resulted in liquid deformable mirrors for adaptive optical control and thus are well-suited for many laser beam shaping applications. Bucaro *et al.*[21] designed a liquid mirror based on self-assembled Janus tiles, which can change the shape of the mirror by electrowetting, and thus tune its focal length. But this mirror could only create a concave or convex deformation. Vuelbanet *et al.*[22] proposed a liquid deformable mirror based on electrocapillary actuation. The proposed mirror offers several advantages, such as a high number of actuators, a high stroke dynamic range, and low cost. However, this mirror is limited by its orientation, thus cannot control the surface deformation accurately. Have *et al.*[23] described a deformable mirror based on the principle of total internal reflection of light from an electrostatically deformed liquid–air interface, which

*Project supported by the National Natural Science Foundation of China (Grant No. 51675321), Shanghai Municipal Natural Science Foundation, China (Grant No. 15ZR1415800), and the Innovation Program of Shanghai Municipal Education Commission, China (Grant No. 14ZZ092).

†Corresponding author. E-mail: zhizhengwu@shu.edu.cn

© 2017 Chinese Physical Society and IOP Publishing Ltd

can produce a large stroke deformation, but is only suitable for the inclined incident light. Déry *et al.*[24] presented a ferrofluid deformable mirror which uses an aluminum-coated reflective PDMS thin film as the mirror surface. These coated membranes have a low surface roughness and high reflectance, but can only produce a small surface deformation with a few micrometers.

Aiming at the deficiency of these wavefront correctors, this paper presents a magnetic fluid deformable mirror (MFDM)-based laser beam shaping technique. This liquid mirror can supply a large surface deformation by superposing a large uniform magnetic field on the small controlled magnetic field generated by the miniature electromagnetic coils underneath. In comparison to other laser shaping techniques, this technique offers the advantages such as simplicity, low cost, large shape deformation, and high adaptability. Based on the fabricated prototype of the MFDM, an experimental AO system for laser beam shaping is set up to produce a desired conical surface shape that shapes the incident beam into Bessel beam. The cross section of the shaped beam is made of concentric annular rings with an intense central spot. Our experimental results have verified the feasibility of the proposed technique for laser beam shaping.

2. Design of magnetic fluid deformable mirror

The schematic diagram of an MFDM is shown in Fig. 1. The proposed deformable mirror uses the magnetic fluids as the driving carrier. The magnetic fluids are stable colloidal suspensions of nano-sized, single-domain ferri-/ferromagnetic particles. When subjected to a magnetic field, the suspended particles affect the flow properties of the carrier fluid, and hence the fluid surface can be deformed by the perturbed magnetic field generated by the miniature electromagnetic coils. In addition, by superposing a large uniform magnetic field to the small perturbed magnetic field, the liquid surface response to the current input of the electromagnetic coils can be linearized and the magnitude of the deflection can be significantly amplified.

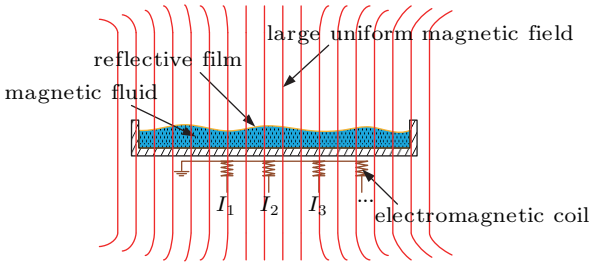


Fig. 1. (color online) Schematic diagram of a magnetic fluid deformable mirror.

2.1. Dynamics model of MFDM

It is assumed that the MFDM is placed horizontally with R the radius of the mirror, d the thickness of the magnetic fluid, h the distance from the surface of the magnetic fluid to the top of the miniature electromagnetic coil, ρ the density of the magnetic fluid, η viscosity, σ the surface tension, χ the magnetic susceptibility, μ the magnetic permeability, and B_0 the uniform magnetic field intensity. In polar coordinates, the time-varying deflection of the mirror surface at sampling point (r_k,θ_k) is denoted by $\zeta(r_k,\theta_k,t)$. The magnetic field generated by the miniature coils in the mirror is idealized as a magnetic potential point source $\psi_j(t)$, $j=1,2,3,\ldots,J$, where J is the number of miniature coils. Define the mode shapes $H_{mnc}=J_m(\lambda_{mn}r)\cos m\theta$ and $H_{mns}=J_m(\lambda_{mn}r)\sin m\theta$, $m=0,1,2,\ldots$, $n=1,2,3,\ldots$, respectively, where J_m is the m order Bessel function of the first kind and λ_{mn} is the eigenvalue for each mode such that $J_m(\lambda_{mn}R)=0$. Then based on the principles of conservation of mass and momentum, and the theories of magnetic field, the mirror surface dynamics equation at any desired location (r_k,θ_k) can be written as[25]

$$\begin{aligned}\zeta(r_k,\theta_k,t) &= \sum_{m=0}^{\infty}\sum_{n=1}^{\infty}\tilde{\zeta}_{mnc}(t)H_{mnc}(r_k,\theta_k)\\ &\quad+\sum_{m=1}^{\infty}\sum_{n=1}^{\infty}\tilde{\zeta}_{mns}(t)H_{mns}(r_k,\theta_k),\end{aligned}\tag{1}$$

where $\tilde{\zeta}_{mnc}(t)$ and $\tilde{\zeta}_{mns}(t)$ are the generalized displacements corresponding to model shapes H_{mnc} and H_{mns}, which are governed by the following two differential equations:

$$\begin{aligned}&\frac{\mathrm{d}^2\tilde{\zeta}_{mnc}(t)}{\mathrm{d}t^2}+4\frac{\eta}{\rho}\lambda_{mn}^2\frac{\mathrm{d}\tilde{\zeta}_{mnc}(t)}{\mathrm{d}t}+\omega_{mn}^2\tilde{\zeta}_{mnc}(t)\\ &=F_{mn}\sum_{j=1}^{J}\psi_j(t)J_m(\lambda_{mn}r_j)\cos(m\theta_j),\end{aligned}\tag{2}$$

$$\begin{aligned}&\frac{\mathrm{d}^2\tilde{\zeta}_{mns}(t)}{\mathrm{d}t^2}+4\frac{\eta}{\rho}\lambda_{mn}^2\frac{\mathrm{d}\tilde{\zeta}_{mns}(t)}{\mathrm{d}t}+\omega_{mn}^2\tilde{\zeta}_{mns}(t)\\ &=F_{mn}\sum_{j=1}^{J}\psi_j(t)J_m(\lambda_{mn}r_j)\sin(m\theta_j),\end{aligned}\tag{3}$$

$$m=0,1,2,\ldots,\quad n=1,2,3,\ldots,\quad j=1,2,3,\ldots,J,$$

with

$$\begin{aligned}\omega_{mn}^2 &= g\tanh(\lambda_{mn}d)\lambda_{mn}+\frac{\sigma}{\rho}\tanh(\lambda_{mn}d)\lambda_{mn}^3\\ &\quad+\frac{\chi}{\rho}B_0^2\tanh(\lambda_{mn}d)\lambda_{mn}^2\\ &\quad\times\frac{\beta\chi\cosh(-\lambda_{mn}h)+\chi^2\sinh(-\lambda_{mn}h)}{\mu\alpha Y(-\lambda_{mn}h)},\\ F_{mn} &= -\frac{\chi}{\rho}B_0\frac{\tanh(\lambda_{mn}d)}{Y(-\lambda_{mn}h)}\lambda_{mn}^2\frac{k}{\pi R^2[J_{m+1}(\lambda_{mn}R)]^2},\\ k &= \begin{cases}1, & \text{for } m=0,\\ 2, & \text{for } m\neq 0,\end{cases}\\ Y(-\lambda_{mn}h) &= -\left(\frac{\mu}{\mu_0}\frac{\beta}{\alpha}+\frac{\chi}{\alpha}\right)\cosh(-\lambda_{mn}h)\\ &\quad+\left(\frac{\mu}{\mu_0}\left(\frac{\alpha}{\beta}-\frac{\chi}{\alpha}\right)-\frac{\chi^2}{\alpha\beta}\right)\sinh(-\lambda_{mn}h),\\ \alpha &= \tanh(\lambda d)-\coth(\lambda d),\end{aligned}$$

$$\beta = \frac{\mu}{\mu_0}\tanh(\lambda d) - \coth(\lambda d).$$

2.2. The structure parameters of MFDM

In order to make the MFDM achieve a large stroke, the Maxwell coil is adopted to produce the large uniform magnetic field and the structure parameters of the miniature coil are optimized through the Taguchi method. The properties of the magnetic fluid used in this paper are shown in Table 1. Based on the analytical model given above, in order to achieve the stroke requirement of 100 μm, the uniform magnetic field intensity is first determined as 7 mT, then the maximum perturbed magnetic field intensity on the mirror surface is calculated to be more than 0.4 mT. The resulting magnetic field distribution of the MFDM is verified by the simulation in the COMSOL Multiphysics software.

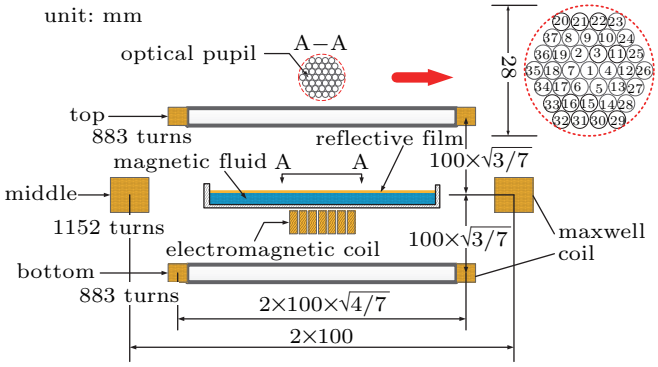


Fig. 2. (color online) Schematic diagram of the prototype MFDM.

Table 1. Parameters of the magnetic fluid.

Parameter	Value
Saturation magnetization	22 mT
Relative permeability	2.89
Density	1190 kg/m^3
Viscosity	3 mPa·s
Thickness	1 mm
Radius	40 mm

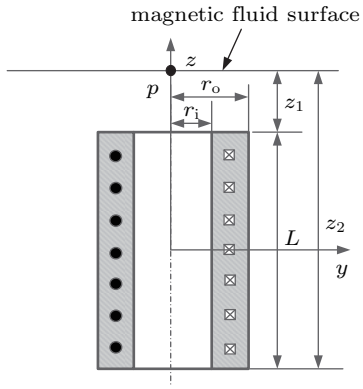


Fig. 3. Structure diagram of the electromagnetic coil.

The mirror is driven using an array of 37 miniature electromagnetic coils arranged hexagonally as shown in Fig. 2. The coils are radially spaced at 4.2 mm from center to center, thus presenting a total active footprint area of approximately 28 mm diameter. In order to satisfy the boundary condition of the magnetic field, the diameter of the mirror container is set as 80 mm. As shown in Fig. 3, the magnetic field at P in the air is given by[26]

$$b_z = \frac{\mu_0 iN}{2L(r_o - r_i)}\left[z_2 \ln\frac{\sqrt{r_o^2+z_2^2}+r_o}{\sqrt{r_i^2+z_2^2}+r_i} - z_1 \ln\frac{\sqrt{r_o^2+z_1^2}+r_o}{\sqrt{r_i^2+z_1^2}+r_i}\right], \quad (4)$$

where r_i, r_o, L, and N are the inner radius, the outer radius, the length, and the number of turns of the electromagnetic coil, respectively, i is the current supplied to the electromagnetic coil, z_1 is the distance between the surface of the magnetic fluid and the top of the electromagnetic coil, and $z_2 = L + z_1$. In this paper, the electromagnetic coil wound with the AWG 38 magnet wire has an inner radius of $r_i = 2$ mm. Then based on Eq. (4), in order to produce a large enough perturbed magnetic field at point P, through the Taguchi method, the length, number of turns, and outer radius of the electromagnetic coil are designed as $L = 8$ mm, $N = 800$, and $r_o = 4$ mm, respectively.

Figure 4(a) shows the magnetic field distribution of the miniature electromagnetic coil. Figure 4(b) shows the magnetic field distribution curve generated by the miniature coil on the mirror surface. It shows that when the input current of the miniature coil is 50 mA, the maximum perturbed magnetic field intensity on the mirror surface can reach 0.7 mT, greater than 0.4 mT.

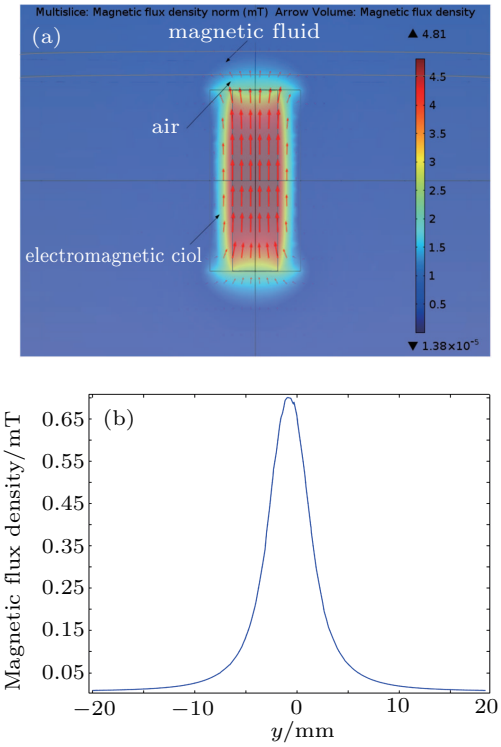


Fig. 4. (color online) (a) Magnetic field distribution of the electromagnetic coil. (b) Magnetic field distribution on the mirror surface.

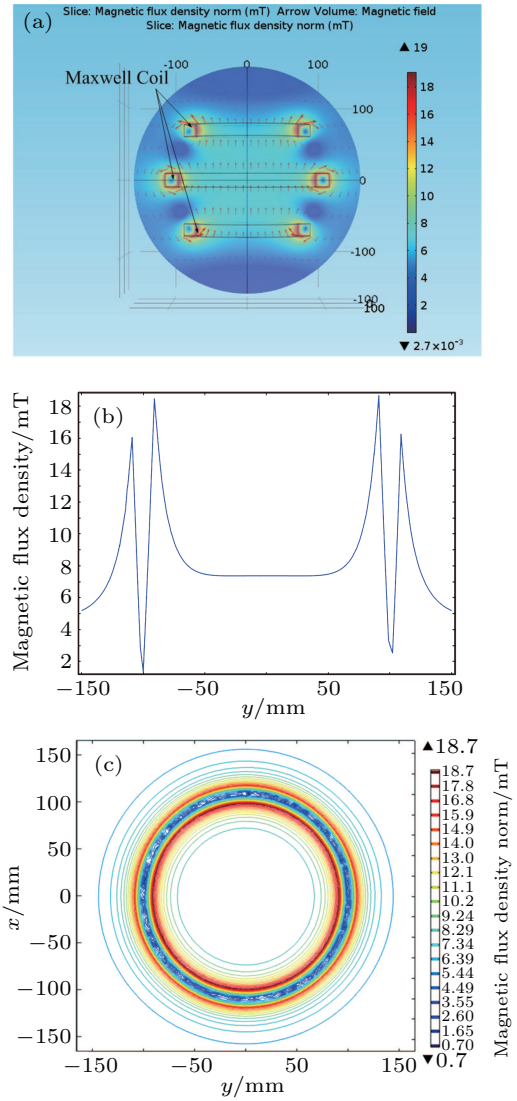


Fig. 5. (color online) (a) Magnetic field distribution of the Maxwell coil. (b) The curve of the magnetic field distribution on the central plane. (c) The equipotential line of the magnetic field distribution on the central plane.

The Maxwell coil is made up of three separated coils which are wound with AWG 25 copper wires. The radii of the three coils and their vertical positions must respect the values given in Fig. 2. The number of ampere-turns of both the lower and upper coils must be exactly in the ratio of 49/64 relative to the middle coil.[27] In this way, the three coils can be arranged in a series circuit and supplied with a single current source. According to the Biot–Savart law, the magnetic field at the center of the Maxwell coil is given by

$$B_0 \approx \frac{15\mu_0 N_m I}{16 R_m}, \tag{5}$$

where N_m is the number of turns of the middle coil, R_m is the radius of the middle coil, and I is the current supplied to the Maxwell coil. In order to meet the requirement of the size of the uniform magnetic field at the center of the Maxwell coil, the radius of the middle coil is set as $R_m = 100$ mm. When $I = 500$ mA, based on Eq. (5), the number of turns of the middle coil is set as $N_m = 1152$, then the numbers of turns of the lower and upper coils are both 883.

The magnetic field of the Maxwell coil is simulated using COMSOL Multiphysics. As shown in Fig. 5(a), the magnetic field inside the Maxwell coil is uniformly distributed. The uniform magnetic field intensity at the center of the Maxwell coil can reach 7.1 mT (see Fig. 5(b)). Figure 5(c) shows that the equipotential line is circular and the diameter is greater than 100 mm, which meet the requirement of the size of the uniform magnetic field.

2.3. Silver liquid-like film prepared for MFDM

Magnetic fluids typically show low reflectance to light and must be coated with metal liquid-like films (MELLFs) that exhibit reflective properties like liquid metals, but are thin enough not to have any significant effect on the deformation of the substrate magnetic fluid. Consequently, a silver liquid-like film has been prepared for the MFDM, which is assembled by a series of processes using encapsulated silver nano-particles as the raw material. There are mainly three steps in the preparation of the silver liquid-like film.

First step 12 mL solution of silver nano-particles was transferred into a centrifuge tube, then dissociated by centrifugation in low speed centrifuge at 3000g for 10 min. After centrifugation, the supernatant was removed, ethanol was infused into the tube, with vigorous shaking for 10 min and then centrifugation again. In order to purify the silver nano-particles, this process was repeated four times.

Second step The obtained silver nano-particles were added to 12 mL ethanol solution, and then mixed with 3 mL dodecanethiol solution by vigorous shaking for 10 min. The mixed solution was kept at room temperature for at least 24 h. The mixed solution was then transferred into a centrifuge tube and centrifuged at 3000g for 10 min. The process could be repeated several times.

Third step 15 mL ethyl acetate was added to the silver nano-particles obtained from the second step, with vigorous shaking for 15 min. The above solution was then dropwisely added to the surface of the magnetic fluid. After the ethyl acetate evaporated, the hydrophobic dodecanethiol encapsulated silver nano-particles automatically stacked and spread on the surface of the magnetic fluid. Finally, a large-scale ordered domain of silver liquid-like film was formed.

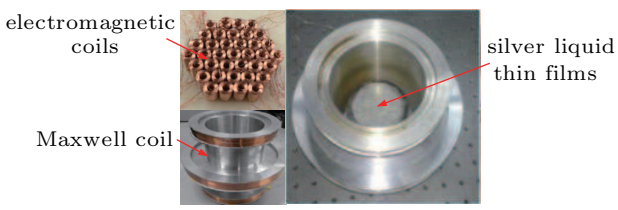


Fig. 6. (color online) Assembly of the prototype MFDM.

In the end, the array of electromagnetic coils, the Maxwell coil, the magnetic fluid, and the silver liquid thin film are assembled together as shown in Fig. 6.

2.4. Thermal effect of MFDM

In some laser beam shaping applications, e.g., the high power laser systems, the thermal effect on the optical elements should be considered. Under the high power laser irradiation, the solid deformable mirror is apt to produce thermal deformation that could influence the output beam quality of the laser systems and even cause permanent damage to the mirror structure.[28] In this section, the thermal effect of MFDM irradiated by the high power laser beam is considered. The temperature distribution and thermal deformation of MFDM are simulated with COMSOL Multiphysics. The model of MFDM built in COMSOL is solved using conjugate heat transfer interface from the heat transfer module that includes a predefined laminar flow and the heat transfer in fluid multiphysics coupling. The model geometry is set up in COMSOL based on the parameters of the MFDM listed in Table 1.

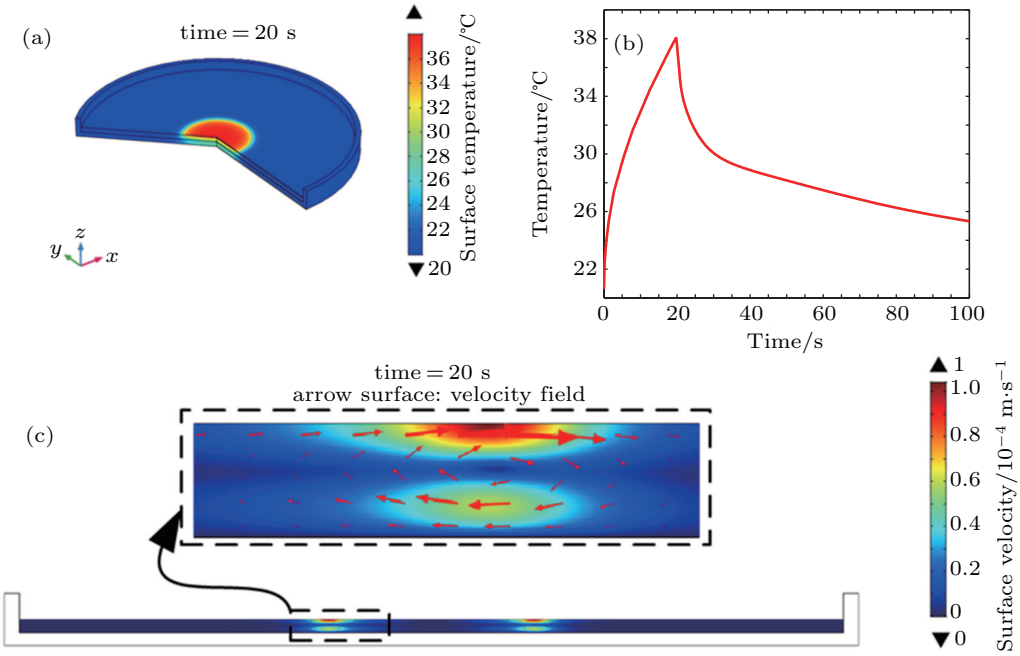


Fig. 7. (color online) The MFDM irradiated by a laser beam with a power intensity of 0.3 kw/cm^2 for 20 s: (a) temperature distribution, (b) variation history of the highest temperature of the MFDM, (c) fluid velocity field.

The mirror surface is supposed to be irradiated by a high-power laser beam incident on the center area of the surface with a power intensity of 0.3 kw/cm^2 at a room temperature of 22 °C. It is assumed that the irradiation time is 20 s and 0.1% of the overall power intensity is absorbed by the magnetic fluid (similar to the energy intensity in Ref. [28]). Figure 7(a) shows the temperature distribution of the MFDM at the end time of 20 s, and it can be seen that the temperature around the center area has risen from 22 °C to 38 °C. Figure 7(b) shows the variation history of the highest temperature of the MFDM. The geometric deformation with the corresponding fluid velocity field at the time of 20 s is illustrated in Fig. 7(c). It can be seen that the temperature change in the fluid causes a slow flow around the edge area of the laser beam and the maximum fluid velocity reaches 0.1 mm/s. However, the mirror surface deformation is quite small and only limited to sub-nanometers. This is mainly due to the slow flow of the fluid that promotes the heat transfer and reduces the thermal stress of the MFDM. It is clear that the stress introduced by the temperature variation inside the MFDM will not cause the damage to the mirror structure, which normally happens to the solid mirrors. However, based on the dynamics analysis of the MFDM in Subsection 2.1, this local slow flow in the fluid may cause limited surface deformation up to ten nanometers when the Maxwell coil is energized. This uncertain perturbation can be effectively eliminated with a closed-loop surface control system.

3. Surface shape control of MFDM

In this section, based on the analytical model developed in Subsection 2.1, the control architecture for the MFDM-based AO control system is presented. First, an augmented plant G is defined to include the MFDM and the wavefront sensor. Based on Eqs. (1)–(3), the MFDM model can be represented in state-space form as $\boldsymbol{P}: \begin{cases} \dot{\boldsymbol{x}} = \boldsymbol{A}\boldsymbol{x} + \boldsymbol{B}\boldsymbol{u} \\ \boldsymbol{y} = \boldsymbol{C}\boldsymbol{x} \end{cases}$ and the corresponding transfer function is denoted as $\boldsymbol{P}(s)$. The deformable mirror introduces a change in the wavefront shape, and the magnitude of this change is twice the magnitude of the mirror shape. The sensor also introduces a delay in the closed loop. Therefore,

the augmented plant is $\boldsymbol{G}(s) = 2\mathrm{e}^{-\tau s}\boldsymbol{P}(s)$, where τ is the sensor delay. By using the Pada approximation, the augmented plant $\boldsymbol{G}$ can be given in state-space form as

$$\begin{aligned} \dot{\boldsymbol{x}} &= \boldsymbol{A}_{\mathrm{g}}\boldsymbol{x} + \boldsymbol{B}_{\mathrm{g}}\boldsymbol{u}, \\ \boldsymbol{y}_{\mathrm{s}} &= \boldsymbol{C}_{\mathrm{g}}\boldsymbol{x}, \end{aligned} \tag{6}$$

where $\boldsymbol{x}$ is the vector of state variables, $\boldsymbol{y}_{\mathrm{s}}$ is the vector of sensor outputs, and $\boldsymbol{A}_{\mathrm{g}}$, $\boldsymbol{B}_{\mathrm{g}}$, and $\boldsymbol{C}_{\mathrm{g}}$ are the system matrices. To reduce the coupling effect of the augmented plant $\boldsymbol{G}$, the DC gain of the MIMO system is considered, which can be obtained as

$$\boldsymbol{G}_0 = \boldsymbol{G}(0) = -\boldsymbol{C}_{\mathrm{g}}\boldsymbol{A}_{\mathrm{g}}^{-1}\boldsymbol{B}_{\mathrm{g}}. \tag{7}$$

Cascading the inverse of the DC gain $\boldsymbol{G}_0^{-1}$ with the augmented plant $\boldsymbol{G}$ yields a system $\bar{\boldsymbol{G}}$ given by

$$\bar{\boldsymbol{G}}(s) = \boldsymbol{G}(s)\boldsymbol{G}_0^{-1}, \tag{8}$$

and results in $\left|\bar{\boldsymbol{G}}(s)\right| = \left|\boldsymbol{G}(\mathrm{j}\omega)\boldsymbol{G}_0^{-1}\right| \approx \boldsymbol{I}$ for $\omega < \omega_0$, where $\boldsymbol{I}$ is an identity matrix and ω_0 is the cut-off frequency of the system bandwidth. The decoupling effect can be more clearly observed in the magnitude response plots for the system $\bar{\boldsymbol{G}}$ given in Fig. 8, which shows the Bode plots for four selected channels (#1, 2, 8, and 20, see Fig. 2). It is obvious that the system is significantly decoupled in the low frequency range.

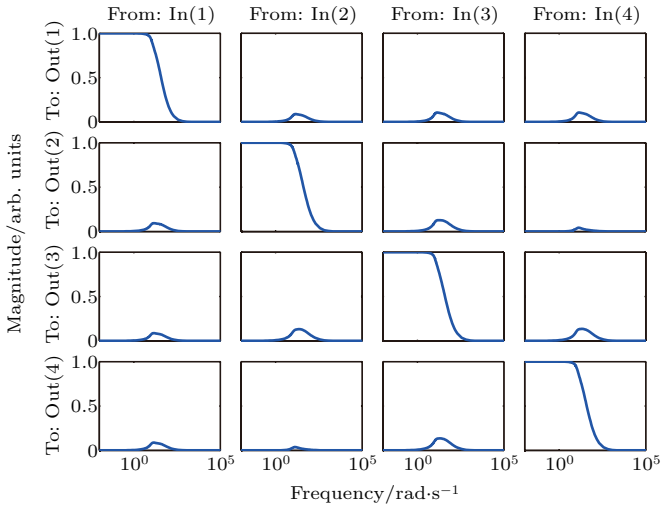


Fig. 8. (color online) Bode magnitude plots of the decoupled plant model.

However, it can be seen from Fig. 8 that the system is not completely decoupled in the high frequency range. Based on the response characteristics, $\bar{\boldsymbol{G}}(s)$ can be approximated as

$$\bar{\boldsymbol{G}}(s) = \bar{g}(s)\boldsymbol{I} + w_{\Delta}(s)\boldsymbol{\Delta}, \tag{9}$$

where the function $\bar{g}(s)$ is the decoupled dynamic model, $w_{\Delta}(s)$ is a band pass filter featured with the un-decoupled frequency range, and $\boldsymbol{\Delta}$ is a constant matrix. In the following, an optimal decentralized lead-lag controller $\bar{\boldsymbol{K}} = k\boldsymbol{I}$ is designed for the system $\bar{\boldsymbol{G}}$, where k is an SISO controller. The overall controller $\boldsymbol{K}$ for the plant $\boldsymbol{G}$ can be written as $\boldsymbol{K} = \boldsymbol{G}_0^{-1}\bar{\boldsymbol{K}}$. Figure 9 shows the control block diagram of the closed-loop system.

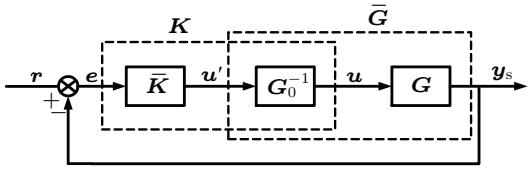


Fig. 9. Block diagram of the closed-loop system using DC gain matrix.

When the signal $\boldsymbol{r}$ is set to zero, the sensitivity function $\boldsymbol{S}_0(s)$ is given by $\boldsymbol{S}_0(s) = (\boldsymbol{I} + \bar{g}(s)\bar{\boldsymbol{K}}(s))^{-1}$ and the system $\boldsymbol{\Sigma}$ is given by $\boldsymbol{\Sigma}(s) = -w_{\Delta}(s)\bar{\boldsymbol{K}}(s)\boldsymbol{S}_0(s)$. Considering the optimal regulation performance of the closed-loop system, the convergence rate of the closed-loop system can be performed by minimizing an H_2 norm as

$$\min_{k} \left\| \frac{1}{s+\alpha}\boldsymbol{S}_0 \right\|_2, \tag{10}$$

with the robust stability condition of the closed-loop system

$$\|\boldsymbol{\Delta}\|\,\|\boldsymbol{\Sigma}\|_{\infty} < 1, \tag{11}$$

where α is a small positive constant. With the designed $\boldsymbol{K}(s)$, $\bar{\boldsymbol{G}}$ can be treated as a collection of SISO systems that can be controlled independently.

4. Experimental results

In this section, the mirror is used to produce a desired conical surface shape for shaping the incident beam into Bessel beam. The pattern of the ideal Bessel beam should be a set of concentric rings with a bright spot in the center. Such beams can be used in a variety of applications, including optical trapping and tweezing, the drilling of high-precision holes, and controlling the propagation of ultra-short pulses in dispersive media. Researchers commonly employed an axicon or conical lens element for the physical realization of Bessel beams, but the parameters of the beam are fixed since the cone angle of a conventional axicon determines the spatial frequency of the beam. The problem can be successfully addressed by using the MFDM, which allows the alteration of the axicon angle.

In order to verify the surface response characters of the MFDM, Polytec OFV 5000/552 and VIB-A-T31 are used to measure the surface deformation. During operation, the Maxwell coil is driven with a constant current of 500 mA, which produces a measured 7 mT uniform magnetic field inside of the Maxwell coil. As shown in Fig. 10, when the center miniature coil (#1, see Fig. 2) is active with 50 mA or −50 mA, the maximum magnitude of the surface deformation can reach more than 100 μm and the coupling between the neighbor coils is about 28% .

Based on the fabricated prototype of the MFDM, an experimental AO system is also set up to evaluate its laser beam shaping performance. Experimental arrangement is illustrated in Fig. 11. The wavefront sensor (Tholabs WFS 150-5C) measures the slope of the incident beam. Then the wavefront slope information is acquired by a PC-based reconstruction and control software, which provides necessary current inputs to the proposed MFDM through an electronic control unit. The CCD camera (Tholabs DCU223C) is mounted on a movable guide rail to collect a series of cross-sectional distributions of the light field.

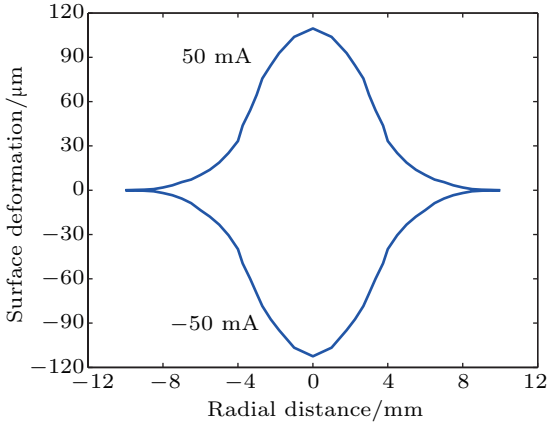


Fig. 10. (color online) The surface deformation of MFDM.

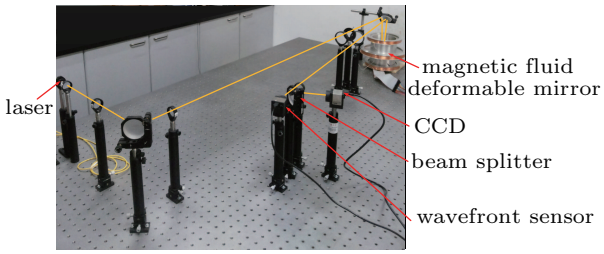


Fig. 11. (color online) Snapshot of the experimental setup.

In the experiment, based on the obtained wavefront slope information, the closed-loop control of MFDM is carried out to produce a static conical surface shape. In the controller design process, the low pass filter $w(s) = 1/(6.944\times10^{-3}s^2 + 1.179\times10^{-1}s + 1)$ is used to filter the sensor noise. For the 37 control channels, based on bode plot analysis of the decoupled system, the uncertainty bound is set as $\|\Delta\|_\infty \leq 3.8$ and the uncertain weight function is selected as $w_\Delta(s) = s/(s+10)$. By using the robust control toolkit in Matlab, the final discrete controller implemented in the computer system with a sampling rate of 15 Hz is designed as

$$\bar{\boldsymbol{K}}(z) = \frac{15.9z^2 - 30.461z + 14.572}{z^2 - 1.933z + 0.933} I_{37\times37}.$$

It should be noted that since in the experimental evaluation it is supposed to create a static conic surface shape to produce a Bessel beam, in the controller design procedure more weight is considered on the robustness than the convergence rate of the closed loop system in order to deal with the uncertainty in physical parameters of MFDM and other possible adverse working environments. The response time of the closed loop system can be dramatically increased if more weight is considered on the convergence rate.

According to the arrangement of the miniature electromagnetic coils, the desired tracking reference value of each channel is set as

$$\begin{aligned}\boldsymbol{r} = [&-12,-8,-8,-8,-8,-8,-8,\\ &-4,-4,-4,-4,-4,-4,-4,-4,-4,-4,-4,-4,\\ &-0.1,-0.1,-0.1,-0.1,-0.1,-0.1,-0.1,-0.1,\\ &-0.1,-0.1,-0.1,-0.1,-0.1,-0.1,-0.1,-0.1,\\ &-0.1,-0.1]^{\mathrm{T}}\ (\mu\mathrm{m}). \end{aligned} \tag{12}$$

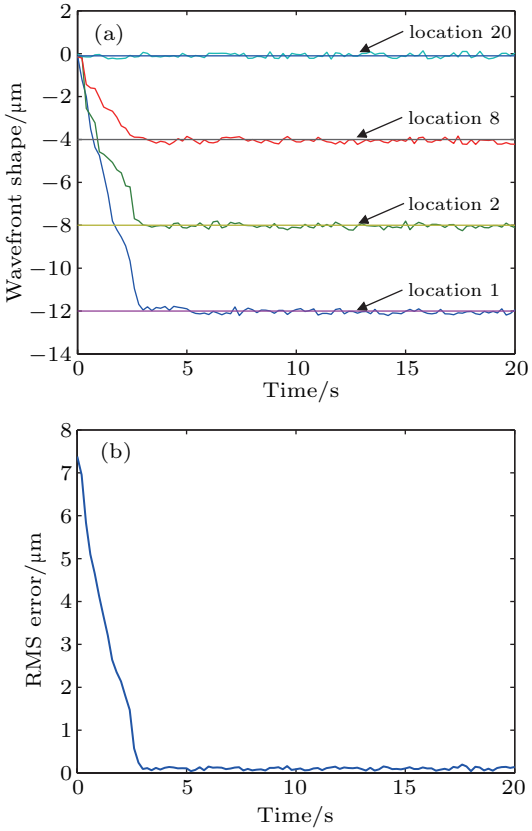


Fig. 12. (color online) Experimental tracking of a static reference shape using decentralized lead-lag controller: (a) wavefront shape, (b) RMS error.

Each entry in $\boldsymbol{r}$ is associated with a spatial location corresponding to the center of one of the 37 coils. To evaluate the performance of the lead-lag controller by tracking a surface shape formed by Eq. (12), figure 12(a) shows the time history of the mirror surface deflections measured at the selected channels (#1, 2, 8, and 20, see Fig. 2). The corresponding reference values are shown as dashed lines. The RMS error in tracking the reference shape is given in Fig. 12(b). The experimental results show a residual steady-state error of 0.28 μm. As can

be observed from the figure, the controller effectively manages to drive the wavefront shape to the desired offset values of the reference shape.

Figure 13 shows a three-dimensional conical surface produced by the MFDM and recorded by the WFS. The spatial profile of the Bessel beam imaged by the CCD camera at different distance along the propagation axis is shown in Fig. 14. A pattern made of concentric annular rings with an intense central spot can be observed clearly. In addition, the dimension of the central spot is invariant along the z-axis and the concentric rings remain at fixed positions, illustrating the non-diffracting character of the produced Bessel beams.

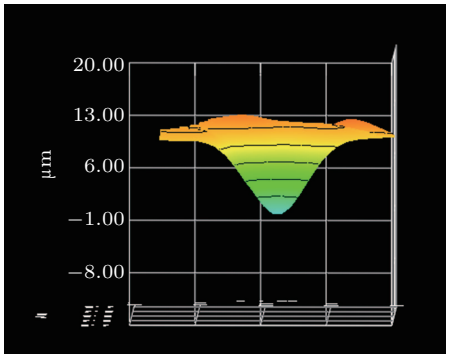


Fig. 13. (color online) Conical surface shape produced by the MFDM and recorded by the WFS.

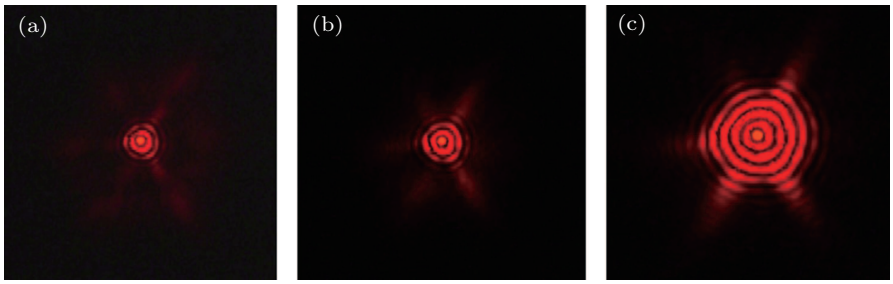


Fig. 14. (color online) Evolution of the spatial profile of the Bessel beam produced by a MFDM axicon along the propagation axis and recorded by the CCD camera: (a) $Z = 45$ mm, (b) $Z = 75$ mm, (c) $Z = 123$ mm.

5. Conclusion

In this paper, a real-time and controllable laser beam shaping technique based on the MFDM has been presented. The liquid deformable mirror using the actuation of the magnetic fluid can easily supply a large stroke more than 100 μm. Firstly, the model of the magnetic fluid deformable mirror is established, and the designed structure of the liquid mirror is presented. Then a decentralized robust control method is proposed for the mirror surface shape control. Finally, based on the fabricated prototype of the MFDM, an experimental AO system for the laser beam shaping is set up to produce a desired conical surface shape that successfully transforms the incident beam into a Bessel beam. These results have verified the feasibility of the proposed technique for the laser beam shaping.

References

[1] Dickey F M 2003 *Optics and Photonics News* **14** 30
[2] Dienerowitz M, Mazilu M, Reece P J, Krauss T F and Dholakia K 2008 *Opt. Express* **16** 4991
[3] Arlt J, Garces-Chavez V, Sibbett W and Dholakia K 2001 *Opt. Commun.* **197** 239
[4] Paterson A, Bauer R, Li L and Lubeigt W 2015 *IEEE J. Selec. Top. Quantum Electron.* **21** 2701007
[5] Dickey F M, Weichman L S and Shagam R N 2000 *Proc. SPIE* **4065**
[6] He J L, Wei L, Yang J S, Li X Q, He Y and Zhang Y D 2016 *Laser & Optoelectronics Progress* **53** 020101
[7] Frieden B R 1965 *Appl. Opt.* **4** 1400
[8] Fan Z M, Li Z and Qian L X 2012 *Infrared and Laser Engineering* **41**
[9] GaoY H, An Z Y, Li N N, Zhao W X and Wang J S 2011 *Optics and Precision Engineering* **19** 1464
[10] Liu Z H, Yang H, Shi Z D, Li G J, Fang L and Zhou C X 2013 *Chin. J. Lasers* **41** 0102005
[11] Yin Z Y, Wang Y F, Yin S Y, Qiang J P, Lei C Q, Sun X H and Yang K 2013 *Chin. J. Lasers* **40** 0602016
[12] Van Wonterghem B M, Salmon J T and Wilcox R W 1995 UCRL-LR-105821-95-1
[13] Yang X T and Fan W 2006 *Acta Optica Sinica* **26** 1698
[14] Liu J S and Taghizadeh M R 2002 *Opt. Lett.* **27** 1463
[15] Wang W 2011 *Laser & Optoelectronics Progress* **48**
[16] Wu F T, Guo D D, Chen Y B and Qiu Z X 2007 *Optics and Precision Engineering* **15** 1692
[17] Li S S, Wang Y L, Lu Z W, Ding L, Du P Y, Chen Y, Zheng Z X, Ba D X, Dong Y K, Yuan H, Bai Z X, Liu Z H and Cui C 2015 *Opt. Express* **23** 681
[18] Yu X C, Hu J S and Wang L B 2012 *Acta Optica Sinica* **32** 514001
[19] Cartella A, Bonora S, Först M, Cerullo G, Cavalleri A and Manzoni C 2014 *Opt. Lett.* **39** 1485
[20] Béchet C, Guesalaga A, Neichel B, Fesquet V, González-Núñez H, Zúñiga S, Escarate P and Guzman D 2014 *Opt. Express* **22** 12994
[21] Bucaro M A, Kolodner P R, Taylor J A, Sidorenko A, Aizenberg J and Krupenkin T N 2009 *Langmuir* **25** 3876
[22] Vuelban E M, Bhattacharya N and Braat J J M 2006 *Opt. Lett.* **31** 1717
[23] Have E S and Vdovin G 2012 *Appl. Opt.* **51** 2155
[24] Déry J P, Brousseau D, Rochette M, Borra E F and Ritcey A M 2016 *Journal of Applied Polymer Science* **133** 44542
[25] 25. Wu Z Z, Iqbal A and Amara F B 2013 *Modeling and Control of Magnetic Fluid Deformable Mirrors for Adaptive Optics Systems* (Berlin: Springer-verlag)
[26] Furlani E P 2001 *Permanent Magnet and Electromechanical Devices* (New York: Academic Press Press)
[27] Caprari R S 1995 *Measurement Science & Technology* **6** 593
[28] Zhang Y P, Fan J Q and Long G Y 2016 *Infrared and Laser Engineering* **45** 1136002